Fragmentation of a liquid metal droplet falling in a water pool

M. Hadj-Achour, N. Rimbert, Michel Gradeck, Renaud Meignen

Fragmentation of a Liquid Metal Droplet Falling in a Water Pool

M. Hadj-Achour,[1] N. Rimbert,[1, a)] M. Gradeck,[1] and R. Meignen[2]
[1)] *Université de Lorraine, CNRS, LEMTA, F-54000 Nancy, France*
[2)] *IRSN (Institut de Radioprotection et de Sûreté Nucléaire), PSN-RES/SAG, France*

(Dated: August 31, 2021)

This paper focuses on the experimental investigation of breakup regimes of a molten fusible metallic droplet in water, at intermediate Weber numbers with emphasis on mass and energy balance. The experiment consists in impacting perpendicularly a molten drop onto the interface of a deep water pool, at a controlled temperature. Using a drop-on-demand device and high speed shadowgraph, a single drop can be visualized during its evolution. There is a noticeable velocity jump when the droplet crosses the interface that can be modeled using unsteady Bernoulli equation. As observed for liquid-gas systems, the drop experiences different regimes of fragmentation, depending on its Weber number: oscillations, bag oscillations, prolate drop stretching breakup and then bowl-shaped bag breakup. However opposite to the gas-liquid case, Rayleigh-Taylor instability mechanism seems to be absent and this seems related to the bowl-shaped bag breakup mechanism when compared to the dome-shaped gas-liquid case. Statistics of the daughter droplets are then given, using either image analysis for large droplets size distribution or sieving and weighting of the solidified fragments for measurement of Sauter Mean Diameter (SMD) and surface energy creation. Lastly, a simple relation between the SMD and the Weber number is presented based on energy and mass balances. When comparing with previous higher Weber number results, a viscous transition corresponding to a strong increase in the energy loss is also shown to occur for the higher Weber number.

I. INTRODUCTION

The breakup of liquid drops has important implications in various fields, like meteorology, aerosol, agriculture, chemical engineering, geology and nuclear safety. Numerous studies[1–5] in the literature were performed with a single liquid droplet surrounded by air (often called secondary breakup). Different experimental approaches have been used in early investigation of secondary fragmentation, such as shock tube (impulsive loading), drop tower (constant acceleration) and wind tunnel.

The parameters governing fragmentation are the Weber number We, the Ohnesorge number Oh,

$$We = \frac{\rho_A U_\infty^2 D_0}{\sigma}, \qquad Oh = \frac{\mu_D}{\sqrt{D_0 \rho_D \sigma}}, \tag{1}$$

the density ratio ρ_R and the viscosity ratio μ_R,

$$\rho_R = \frac{\rho_D}{\rho_A}, \qquad \mu_R = \frac{\mu_D}{\mu_A} \tag{2}$$

where ρ_A is the ambient liquid density, ρ_D the liquid drop density, U_∞ the initial relative velocity between the water and the drop, D_0 the liquid drop initial diameter, σ the surface tension, μ_D the droplet liquid dynamic viscosity and g the acceleration due to gravity. Other relevant numbers are often used, e.g. the Eötvös number (Eo) and the Reynolds number (Re),

$$Eo = \frac{\Delta\rho g D_0^2}{\sigma}, \qquad Re = \frac{\rho_A D_0 U_\infty}{\mu_A}. \tag{3}$$

The Eötvös number is the ratio between the Archimedean force and the surface tension, while the Reynolds number governs the wake of the droplet.

In studies of secondary breakup, gas-liquid experiments are the most numerous[6,7]. The most important parameter has been found to be the Weber number. Based on the breakup morphology, the breakup modes of secondary fragmentation have been termed vibrational ($We \leq 11$), bag-breakup ($11 \leq We \leq 35$), multi-mode or "bag and stamen" ($35 \leq We \leq 80$), shear stripping ($80 \leq We \leq 350$), catastrophic ($We \geq 350$). This regime map was based on observations obtained from experiments of liquid drop breakup in gas streams[2]. Moreover[8], for a droplet in an air stream, the effect of drop viscosity is not significant when the Ohnesorge number based on the drop properties is less than 0.1. The drop size distribution for the bag breakup has been examined[1] and it has been shown to be made up of a large number of small drops produced by the burst of the bag and a few large drops from the breakup of the annular rim, thought the exact size Probability Density Function (PDF) of daughter droplets is still debated. Recently, the deformation and breakup of a drop into a continuous air-jet has been investigated[9] using PIV. The generation of alternating vortices behind the drop eventually affects the bag morphology.

Comparatively, fewer works have investigated the breakup of liquid metal drop in a surrounding liquid[6,10–12]. Some Liquid-gas works however contain data on liquid-liquid systems[2]. Experiments using an exploding wire technique[11], reported that liquid-liquid fragmentation modes were different from those observed in liquid-gas systems. In the review paper of Gelfand[6], four different breakup modes for a liquid-liquid system are proposed based on experimental data found in the literature (mostly conference proceedings). He did not name these modes, as the very distinct intermediate breakup modes of gas-liquid atomization (bag, bag and stamen, ...*etc.*) were not observed and the other modes were otherwise quite similar; the main difference being the erosion of the droplet that happens sooner when the Weber number is increased. More recently, fragmentation of a large liquid gallium drop in water has been studied[13] and liquid-liquid cases with low density

[a)] Electronic mail: nicolas.rimbert@univ-lorraine.fr

ratio[14] have been studied with an emphasis on applying turbulent entrainment theory[15].

In this paper, we describe experimental results on the breakup of a molten metallic drop into a water pool at low Ohnesorge number and moderate Weber numbers. In our experiments the density ratio is constant and equals roughly eight. All other parameters are kept constant (for instance $Oh \approx 0.0028$), except the Weber number which ranges from 10 to 118 and the Reynolds number which therefore varies from 3986 to 13809. Our main objective is to characterize the different fragmentation regimes, to provide a global energy balance and to develop a correlation for the characteristic size of fragments that can be used in nuclear safety modelling code like MC3D[16,17]. A focus is therefore put on the origin of the differences between gas-liquid and liquid-liquid experiments which seems linked to the absence of Rayleigh-Taylor instability mechanism in the present case. An analytical model for the velocity jump across the interface is devised but the main findings of the present work are the derivation of the correlations for the Sauter Mean Diameter of fragments as a function of the Weber number of the mother droplet from a balance of mass and energy before and after breakup and the existence of two distinct effective characteristics Weber numbers of the fragments for the gas-liquid and the liquid-liquid cases.

The remainder of the paper is organized as follows: A general description of the experimental method is presented in Section II. In Section III, the experimental results are given and analysed with an emphasis on description of the different mechanisms (velocity jump, drop deformation, instability and size distribution of the fragments). Lastly, in section IV, scaling of the fragments' size with the Weber number is studied and a model using mass and energy balance during fragmentation gives part of the explanation for the difference between gas-liquid and liquid-liquid cases.

II. EXPERIMENTAL SETUP

A. Material

Experiments were done using Field's metal, which is a fusible alloy with a melting point of 62°C. It is a eutectic alloy of bismuth, indium, and tin, with the following weight percentages: 32.5% Bi, 51% In, 16.5% Sn. As it contains neither lead nor cadmium, it is a non-toxic alternative to Wood's metal. Liquid metals exhibit generally remarkable mechanical properties, in particular high surface tension and low viscosity. Some authors have recently reported them as yield stress fluids[18] and this may be related to surface oxidation[19]. To limit oxidation, nitrogen is used in the injector and air is removed from the pool by injecting nitrogen before the experiment. However oxidation cannot clearly be ruled out as the experiment is not enclosed in a glove box filled with pure nitrogen. Rheological measurements performed in the laboratory have shown that the liquid metal exhibits a non-Newtonian behavior even when under nitrogen or argon atmosphere. A flow threshold was indeed observed around 0.1 Pa. However, this value is small enough to consider that this yield stress effect, whether related to the bulk or to the skin of the liquid has no effect on the deformation of the droplet once it penetrates into the water. It does however govern the initial shape as the created droplet is not fully spherical and possesses a tail, see Figure 1. Actually, its shape is quite similar to other yield-stress fluid droplets[20].

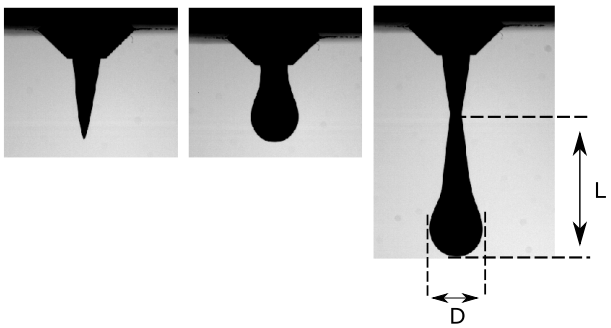

Figure 1: Snapshots of a produced droplet from a 2 mm diameter nozzle.

In present work, most physical properties of Field's metal have been measured or their values verified in the lab.

The interfacial tension between metal and water was measured by a variant of the ADSA method (axisymmetric drop shape analysis). ADSA methods[21] are based on the numerical fit between the shape of experimental drops (or bubbles) and the mathematical model given by the classical Laplace equation. The method proposed by Hansen and Rodsrud[22], which has been used here, is simpler as surface tension can be obtained from a simple geometrical fitting of the drop by an osculating circle (*cf.* Appendix B). The reason behind our own measuring of the surface tension is that it is know to be quite sensitive to the oxygen content of the drop (which act as a tensio-active) and also, to a lesser degree, to the temperature[23,24]. The measured interfacial tension obtained is therefore an effective value, taking into account value the presence of a potential oxide layer and the influence of temperature. The surface tension water-metal measurement was achieved at a droplet contact temperature of 75 °C (*q.v.*). The value that we obtained is similar to the value obtained by Kouraytem *et al.*[25] and this may be related to similar operating conditions and a very small sensitivity to temperature (usually[23] $d\gamma/dT \approx 10^{-4} - 10^{-3} N.\mathrm{m}^{-1}.K^{-1}$ and the surface tension of metal is relatively high and our variations of temperature are relatively small).

Melting heat and heat capacity were measured by Differential Thermal Analysis (DTA)[26]. Measurements of mechanical and thermal properties obtained at the laboratory are given in Table I. Conductivity is assumed to be $18.5\mathrm{W/m/K}$, as measured by Lipschitz *et al.*[27], 25°C above melting point.

ρ	σ	μ	L_v	C_p	κ
kg/m^3	N/m	Pa.s	$\frac{J}{kg}$	$\frac{J}{kg.K}$	$\frac{W}{m.K}$
7994	0.41	0.01	26415	300	18.5

Table I: Physical Properties of Field's metal. ρ is the density measured at ambient temperature, σ is the water/liquid metal interfacial, μ is the dynamic viscosity, each measured at 75°C, L_v is the fusion latent heat measured by DTA and C_p the heat capacity, which do not vary much in the range $40-80$°C. κ is the thermal conductivity obtained from Lipschitz *et al.*[27],

B. Experimental procedure

1. Experimental setup

Our experiment consists in a molten drop impacting perpendicularly by gravity onto the horizontal surface of a deep water pool. The experimental setup is shown in Figure 3. The contact interface temperature (*q.v.*) of molten-water was set at 75 °C, thirteen degrees above the melting temperature of 62 °C to guarantee that solidification has limited impact during the breakup process. At the end, debris are collected and sieved.

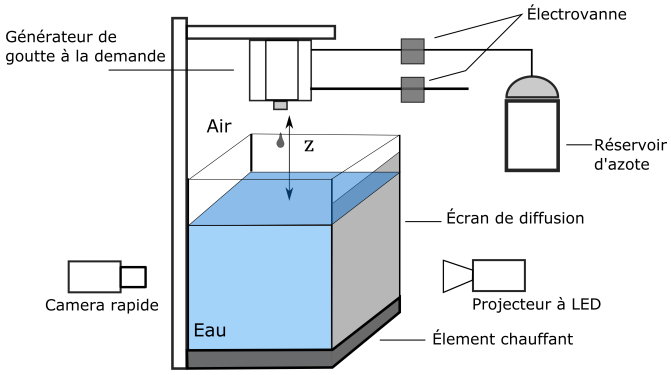

Figure 2: Experimental setup.

The experimental setup includes a water pool, a pneumatic drop on demand generator, a LED lighting, a nitrogen gas tank, a regulating heating-element and a data acquisition system coupled to a high speed camera (phantom V701).

To produce a single metallic droplet, a pneumatic drop-on-demand generator was designed; it is inspired by the work of[28]. Modifications were made to the original design, such as replacement of the cartridge heater. The temperature was maintained constant using a "double boiler" system. A grid was added at the nozzle exit to obtain a uniform flow during the formation of the droplet, see Figure 3.

The generator was connected to a nitrogen supply kept at 4 bars as shown in Figure 3. When the solenoid valve is opened, the overall pressure increases in the container of liquid metal, which results in droplet formation at the nozzle.

High-speed shadowgraphy is used to visualize the droplet/liquid interaction with a maximum resolution of 40 µm/pix. Time-resolved visualization of the droplet deformation requires having a high acquisition rate (8000 Hz). In order to obtain high contrast images and high resolution with a short time exposure, a bright light LED panel source is used (PRIOLITE LED 400 equivalent to a 400W halogen light output). To make appropriate statistics, over 200 runs are made for each trial condition. An averaged value of the initial drop weight m_0 (equal to 0.27 g $\pm$ 0.01 g) is obtained with an equivalent mass diameter D_0 equal to 4 mm, according to the relation,

$$D_0 = 2\left(\frac{3}{4\pi}\frac{m_0}{\rho_D}\right)^{1/3} \tag{4}$$

For each trial we have determined an height-to-width aspect ratio H_0/W_0 (see Figure 1) for the initial droplet. The mean value is 2.04 with a maximum dispersion equal to 4%. Note that, assuming an initial prolate spheroidal shape with the same aspect ratio, this results in a 7% increase of the surface and therefore in a 7% systematic underestimation of the Weber number (since some surface energy is stored in this initial deformation *cf.* Appendix A).

2. Experimental method

The impact velocity used in our experiment is the terminal fall velocity of the droplet before it penetrates water, which gives,

$$U_\infty = \sqrt{2gz} \tag{5}$$

z is the falling height (*cf.* Figure 3), the values are given in Table II. Note that in the range of droplet height before impact considered here (less than 120 cm), the friction forces with air are negligible.

Moreover, since the stem valve is tightly closed so that only the initial pressure pulse allows for the droplet to form, the initial velocity can be assumed to be zero.

The dimensionless time t^* is calculated as the ratio of the physical time t to the characteristic breakup time t_{RN}, defined by[29] as follow,

$$t_{RN} = \frac{D_0\left(\frac{\rho_D}{\rho_A}\right)^{1/2}}{U_\infty}, \tag{6}$$

$$t^* = \frac{t}{t_{RN}}. \tag{7}$$

Since $Oh = 0.008 \ll 0.1$, we expect viscosity to have a negligible influence on the fragmentation regime[6]. After carefully delimiting the fragmentation regimes (by increasing the fall, centimetre by centimetre), experiments have been conducted

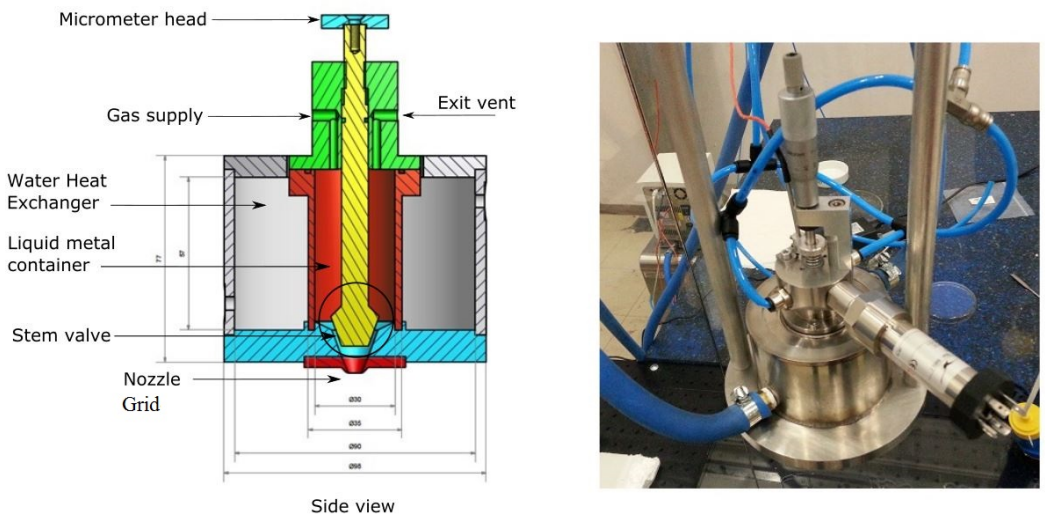

Figure 3: Drop on demand device. The liquid metal is contained in the red part (online version) while gas is supplied and exits through the green part (online version). The yellow (online version) stopper rod is slightly open preventing dripping when a gas over-pressure is not provided.

for eight different falling heights (and henceforth eight Weber numbers), with a constant Eötvös number of 1.54. These can be found in table II which also gives the observed drop acceleration and the measured wavelength of instabilities. The acceleration a ($\mathrm{m/s^2}$) was estimated by measuring the drop motion from digital camera using at least three successive pictures. The dimensionless instability wavelengths λ/D_0 are also obtained by visualization (*cf.* Figure 10). The determination of the wavelength has been done manually by carefully choosing an image where they were apparent; therefore, leading to an operator induced bias. Moreover, the large field of view and the small resolution of the camera lead to an high uncertainty which has been estimated to be around 30% on the average.

To measure the size distribution of the daughter droplet as accurately as possible, two complementary methods have been used. The first one is a very simple and ancient method[12,30,31]: the droplets are frozen by the surrounding water pool and sieved at the end. The second method resorts to image analysis using high-speed shadowgraph.

Considering the solidification method, in order to determine the proper temperature, for an initial liquid metal temperature of 85 °C, the pool temperature has been increased from ambient temperature to the limit where droplets were still liquid when they touched the bottom (50 °C) . Therefore an inferior value, of 40 °C, has been used for the pool temperature in most experiments to ensure that the fragments do not coalesce on the bottom (this value is actually limited by the height of the $50 \times 50 \times 40$cm pool as using a deeper pool would allow for a higher bath temperature). This corresponds to a contact temperature T_C of about 76 °C, obtained by the following equation (neglecting convection),

$$T_C = \frac{E_D T_D + E_A T_A}{E_D + E_A} \tag{8}$$

where E_D and E_A are respectively the thermal effusivity ($\sqrt{\kappa \rho C_\mathrm{p}}$) of the Field's metal droplet and ambient water, T_A is the ambient water pool temperature and T_D is the Field's metal droplet temperature. As melting temperature of Field's metal is equal to 62 °C, this contact temperature should be high enough to prevent solidification to influence fragmentation while still getting solidified fragments that can be sieved. Using a lower pool temperature, for instance (20 °C), permit to freeze the droplet during deformation into bag and before fragmentation, *cf.* Figure 4. Notice the shape of the bag which seems to wrap around itself. The frozen daughter droplets are then dried and sieved using a Retsch vibratory sieve shaker AS 200 with sieving diameters, $D_i \in \{20\mu\mathrm{m}, 50\mu\mathrm{m}, 100\mu\mathrm{m}, 500\mu\mathrm{m}, 1000\mu\mathrm{m}, 2000\mu\mathrm{m}\}$.

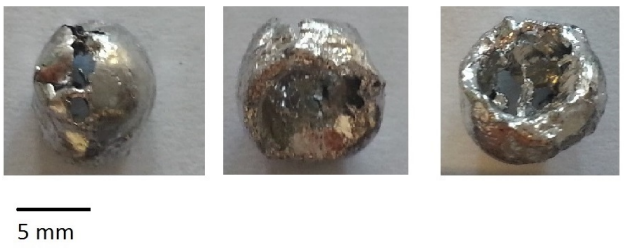

Figure 4: Frozen droplet during the bag formation stage, for We = 40, T_D = 85 °C and T_A = 20 °C.

Particle counting was also performed by image processing using (ImageJ, http://imagej.nih.gov/ij/) but this restricts the PDF to droplets larger than the pixel equivalent size (i.e. 40

	z (cm)	U (m/s)	Re	t_{RN} (ms)	a (m/s^2)	λ/D_0
$We = 118$	60	3.43	13809	5.5	- 610	0.266
$We = 99$	50	3.13	12606	6.3	- 482	0.309
$We = 79$	40	2.80	11275	7.9	- 385	0.421
$We = 59$	30	2.42	9765	9.7	- 193	0.573
$We = 39$	20	1.98	7973	12	- 161	0.6
$We = 20$	10	1.40	5637	/	- 129	/
$We = 10$	5	1.00	3986	/	- 64	/

Table II: Initial conditions for the different experiments and the corresponding Ranger and Nicholls characteristic time.

μm) and neglect out of focus particles (and to a lesser extent, crossing particles but they are negligible in the present case). Therefore it can be inferred that (owing to Shannon's theorem) above 2.2 times the pixel size *i.e.* 90 μm, this method begins to produce accurate estimates of particles diameter distribution. The procedure begins with a normalization of the images; this stage aims at obtaining a uniform background of the image. Then, based on the droplet surface area A, an equivalent diameter d is estimated using the following expression:

$$d = 2\sqrt{A/\pi} \tag{9}$$

Therefore, the PDF is accurate for spherical droplet only These two methods have their advantages and disadvantages. On the one hand, sieving is mass preserving so that no droplet is theoretically unaccounted for (thought collection of very fine powder may be hard). Its precision is limited by the range of sieves used. Moreover, the smallest sieve used (20 μm) is much smaller than the smallest pixel so small droplets should be more precisely taken into account using this techniques. Let us emphasize that smaller droplets having larger surface to volume ratio, they are very important when computing the Sauter Mean Diameter (which is the diameter of the droplet with the same surface to volume ratio as the whole cloud). On the other hand, the image processing technique allows us to choose the size of the bins and produce therefore a much smoother PDF which can then be compared with classical PDF shape and maybe understand underlying mechanisms. To conclude with this comparison, the sieving technique is expected to produce no bias in the measurements (but unfortunately with large uncertainties as the sieve sizes are large) while the image analysis should give smooth PDF but where bias, due to lack of mass conservation and limited range, cannot be ruled out. They therefore complement each other relevantly.

III. EXPERIMENTAL RESULTS AND PHENOMENOLOGICAL ANALYSIS

A. Impact on the Pool Surface and Velocity Jump

Figure 5 shows the typical impact of a molten drop on the water pool surface. For the range of Weber numbers considered in the experiments, no air cavity and no bubble trapping in the pool are observed when the molten drop penetrates the air-water interface. However the droplet decelerates when it crosses the interface as can be seen in Table III and figure 6. Appendix E gives an estimate of such a velocity jump using the unsteady Bernoulli equation (as the drop begins to deform when it crosses the interface, the unsteady formulation is needed) and it is shown to be

$$\frac{U_D}{U_A} \approx \rho_R^{-3/4}, \tag{10}$$

where $U_A = U_\infty$ is the ambient fluid velocity seen from the droplet frame of reference before the impact and $U_D = U_\infty - U_+$ is the velocity of the droplet after the shock in the same frame. In our case, this is constant and equal to 0.23 in the case of a density ratio equal to 8, quite in agreement with present results (using steady Bernoulli equation would lead to a velocity jump intensity of 0.35). This also implies that the corrected Weber number We^* computed with the velocity U_+ of the droplet after the interface crossing would be roughly equal to $(1-0.23)^2 \approx 0.59$ time the initial Weber number.

B. Breakup regimes

Figure 10, shows a closer look at the various possible shapes of Field's metal obtained in the experiment. For the lower Weber numbers the drop oscillates. It still shows few breakup at Weber numbers ranging between 8 and 30. When it does not break, it has been noticed that its equilibrium shape is not spherical and large amplitude oscillations are present. It can be seen on figure 7 the breakup of a droplet in exactly two parts for $We = 21$ but this was an exception as more fragments are usually produced. To have an order of magnitude of the fragmentation ratio , it can be seen on table V in Appendix C that for Weber number 10, $59.623/60.231 = 99\%$ of the initial mass is still in the larger sieve of 2mm (and most corresponds to unbroken droplet), the result is still $57.069/60.050 = 95\%$ for Weber number 20 but decreases to $42.708/59.952 = 71\%$ for Weber number 39. For larger Weber numbers (*i.e.* above 50), there are no more oscillations and the drop takes the form of a cap or a hollow bag and subsequently the thin cap breaks up into small droplets every time. The different regimes of deformation and fragmentation are summarized in Figure 8.

Some similarities can be drawn between liquid-gas and liquid-liquid systems. For liquid-air systems, the bag breakup regime can be divided into four stages[32]. Here, during the initial stage, the drop deforms into a dome shape. In the next stage, a hollow bag is formed, which is attached to a

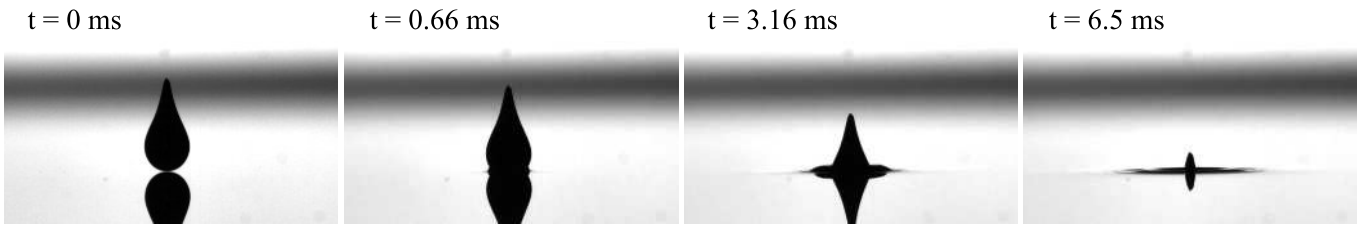

Figure 5: The drop impact on air-water interface. 600 Hz data acquisition

We	U_∞	U_+	$\Delta U/U_\infty = (U_\infty - U_+)/U_\infty$
10	0.9	0.9	0.00
20	1.35	1.17	0.13
39	1.95	1.44	0.26
59	2.43	1.8	0.26
79	2.8	2.07	0.26
99	3.13	2.16	0.3
118	3.43	2.19	0.36

Table III: Velocity Jump when the droplet crosses the pool interface, U_∞ is the initial velocity and U_+ the velocity after the crossing of the interface.

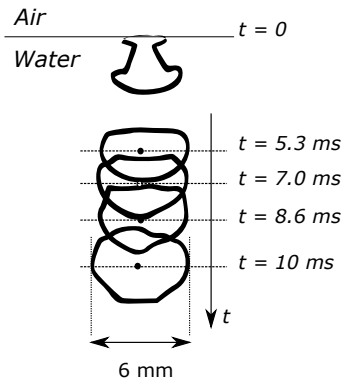

Figure 6: Velocity jump and acceleration calculation.

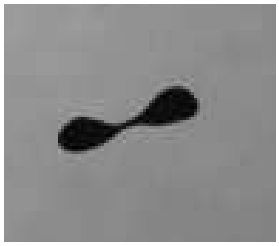

Figure 7: $We = 21$ breakup of a droplet into two equals parts. Heating of the surrounding fluid leads to a slight blur around the droplet.

toroidal rim. Subsequently the thin bag breaks up into small droplets leaving behind an intact rim. Finally the rim breaks up into large droplets owing to some capillary instability, as illustrated in Figure 9. Therefore the same four stage are recovered, the main difference being the orientation of the bag: here the droplet is curved toward the rear (or "bowl" shape)

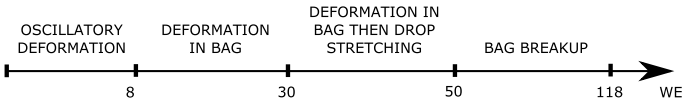

Figure 8: Deformation and fragmentation regimes obtained in the present experiments.

while in gas-liquid experiments it is curved toward the front (or "dome" shape).

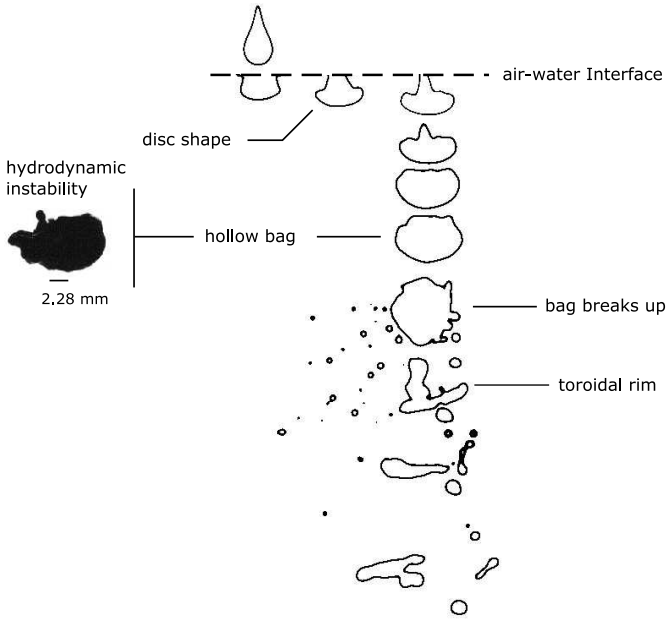

Figure 9: Drop deformation for We = 59.

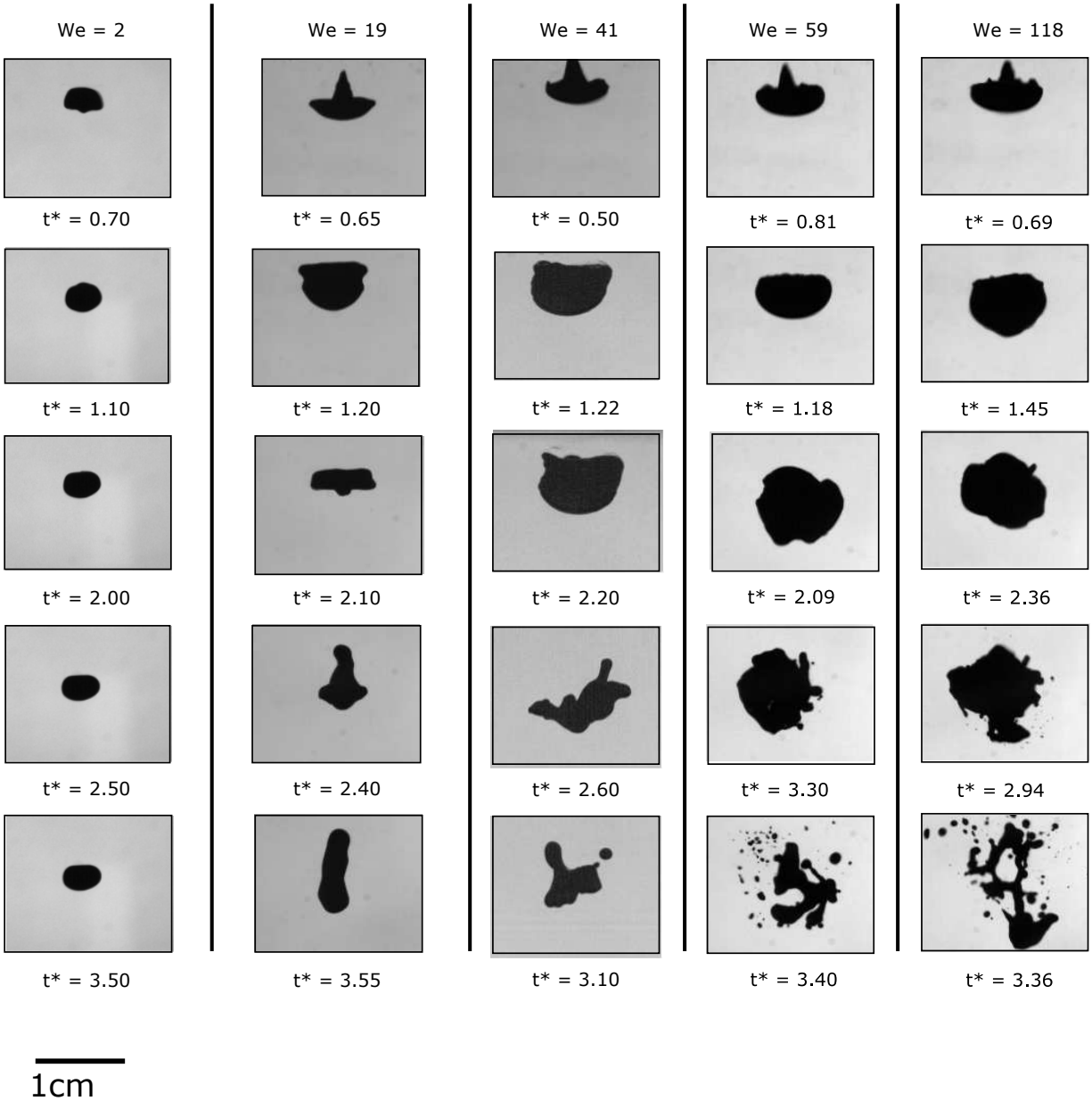

Figure 10: Drop immersed in the water pool. From left to right, oscillations, bag and prolate oscillations, bag oscillation and breakup, bag breakup.

C. Droplet Deformation

In order to understand the discrepancy between gas-liquid and liquid-liquid systems, let us recall the mechanism of drop deformation and breakup is governed by interplay of hydrodynamic pressure and capillary or viscous forces. The deformation is essentially caused by hydrodynamics pressure, whereas capillary forces and viscous forces, respectively, resist and delay drop deformation. However, for low Ohnesorge numbers ($\ll 0.1$), as is the case in this study, the viscous forces have a negligible role on the drop deformation.

The droplet deformation over time was estimated using image analysis (thanks to imageJ). The dimensionless cross stream deformation $W^* = W/D_0$ is defined by the width W of the smallest rectangle containing the drop, normalized by the initial mass equivalent drop diameter D_0. Measurement of the bag deformation as function of the dimensionless time t^* in the transverse direction to the flow is given in Figure 11. The most striking point here is that the non dimensional drop deformation measurements are mostly independent of the Weber number. The dimensionless cross stream deformation increases linearly during the first instant (*i.e.* up to $t^* = 0.3$) and then slowly increases in what could be supposed to be a slow second linear regime where it saturates at around $t/t^* = 1.8$ with a maximum deformation close to $W^* \approx 2$.

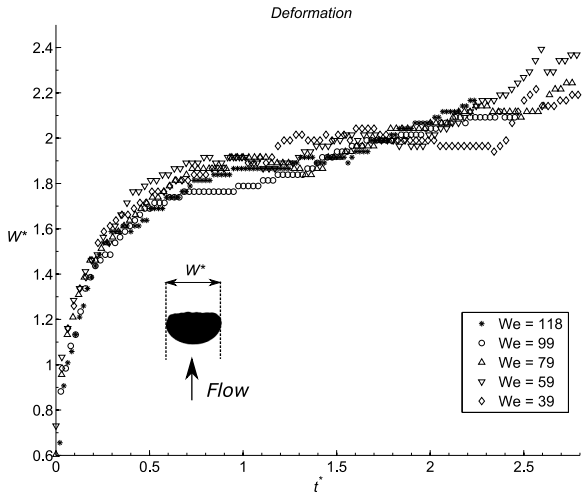

Figure 11: The dimensionless cross stream deformation

1. Initial Deformation

This can be explained by revising the fundamentals of drop/globule deformation in an outer flow[4,33–35]. The main governing parameter is the pressure difference between the pressure P_+ at the stagnation point located at the front of the droplet (in its frame of reference) and the lower pressure P_- on the edge of droplet due to the velocity increase of the outer flow. Using Bernoulli relation, this pressure difference can be approximated as $P_+ - P_- \approx \zeta^2 \rho_A U_\infty^2$, where $\zeta = U_-/U_\infty$ is the velocity increase ratio on the edge of the drop (its value is 1.5 for a spherical droplet[36] and shall strongly increase when the droplet deforms). Neglecting surface tension, this pressure difference creates a velocity $V \approx \zeta\sqrt{\rho_A/\rho_D}U_\infty$ inside the droplet leading to its deformation with a characteristic time scale given by t_{RN} (*cf.* equation 6). It can therefore be assumed that

$$\frac{dW}{dt} \approx V \approx \zeta\sqrt{\frac{\rho_A}{\rho_D}}U_\infty. \tag{11}$$

In the beginning $\zeta(W)$ varies slowly so that the non-dimensional deformation velocity dW^*/dt^* can be assumed to be a constant B *i.e.* an effective value of ζ. With this hypothesis, the deformation of the droplet should be linear in time and independent of the Weber number.

$$W^* = W_0^* + Bt^* \qquad 0 \le t^* \le 0.3 \tag{12}$$

This can be seen in many experiments[37,38]. Correlation (12) is in good agreement with the present experimental results (*cf.* figure 11), when B equals to 2.5 which is slightly larger than the spherical drop value of 1.5, as expected. However, it stops after roughly $0.3t_{RN}$ and it can be seen that, soon after, the maximum deformation is reached with value close to 2 after which the drop fragments. Fragmentation happens quicker for the higher Weber number (and the curve is then stopped) but we do not have enough (proper) statistics and we decided to skip this analysis. This long time similarity may be related to the vortex ring building up in the wake of the droplet and governing the sheet wrapping of the droplet, eventually leading to its fragmentation.

This seems to be valid in all breakup regimes (before fragmentation begins) and seems to be almost independent with the Weber number. This value of 2 is also the deformation value preceding the breakup in many gas-liquid cases[2].

2. Bag Shape and Dome to Bowl Transition

The main difference between liquid-gas and liquid-liquid metal is the bag direction: for the metal-water system, it is in the opposite direction to the flow, whereas for the water-air system, it is in the same direction as the flow, they are called respectively bowl-shaped and dome-shaped. This transition is sometimes related[2] to the ratio between shear stresses to surface tension stresses, and the bowl shape is obtained when the former is greater than the latter. However, a closer examination of the data published[2] shows that all bowl shapes are liquid-liquid experiments while all dome shape are gas-liquid experiments. Actually some liquid-liquid data points were reported[2] to be domes (for water/oil system); but these points were measured for Weber numbers less than 2 where the droplet does only oscillates. Therefore, if these points are removed the density ratio seems to be the main governing parameter determining this shape transition. The goal of the following is a tentative explanation of this fact in three steps.

Firstly, the evolution equation for the relative velocity U_r between the droplet and the surrounding fluid reads (neglecting added mass or other effects like Basset term...)

$$\frac{1}{U_r}\frac{dU_r}{dt} = -\frac{3}{4}\frac{\rho_A}{\rho_D}C_d\frac{Ur}{2R_0} \tag{13}$$

So that the characteristic time for the velocity equilibration t_e (a very similar/proportional form is sometimes called the acceleration time[6]) is different from t_{RN} and reads

$$t_e = \frac{\rho_D}{\rho_A}\frac{2R_0}{U_r} \tag{14}$$

Therefore the ratio between the two characteristic times scales as

$$\frac{t_e}{t_{RN}} = \sqrt{\frac{\rho_D}{\rho_A}} \tag{15}$$

In the present case, ratio (15) equals approximatively 2.8. In gas-liquid experiments this ratio is very large, meaning that the drop velocity does not adjust during fragmentation and therefore few momentum is exchanged with the surrounding; while in liquid-liquid experiments this ratio is closer to unity and there is a stronger momentum exchange with the surrounding.

Secondly, approximate value of the drag coefficient can also be inferred from formula (13) considering that[34]

$$C_d \approx \frac{8}{3}\frac{\rho_D}{\rho_A}\frac{R_0}{W^{*2}}\frac{a}{U_+^2} \tag{16}$$

Using acceleration values given in table II and assuming $W^* = 2$ lead to values ranging from 0.65 to 1.35 for C_d, closer to the drag of a disk than a sphere. Therefore, it can be supposed that contribution from flow separation is important in the value of this drag coefficient. As this flow separation is mostly linked to the creation of a vortex ring in the wake of the droplet[14,39,40], this is, to our understanding, the best explanation for the difference between liquid-liquid case and gas-liquid experiments: a very strong vortex ring is generated in the wake of the drop in the liquid-liquid case precluding the appearance of Rayleigh-Taylor instabilities as can be seen in next section (which constitutes the third part of our explanation).

3. Possible Instability Mechanisms

Many authors[10,14,41–44] suggest that the Rayleigh-Taylor instability plays an important role in drop breakup mechanisms and can be considered as criterion of breakup. In this hypothesis, when the characteristic size of the drop D_{max} is larger than the critical wavelength λ_{RTmax}, the Rayleigh-Taylor instability is assumed to grow in the drop leading to an eventual bag breakup. However, Kelvin-Helmholtz instability is also often mentioned as a source of instability[45], mainly associated to the shear breakup. Let us therefore compare these two possibilities. First, the wavelength of the most unstable Rayleigh-Taylor wave is expressed as,

$$\lambda_{RT,max} = 2\pi\sqrt{\frac{3\sigma_L}{|a|(\rho_D - \rho_A)}} \tag{17}$$

where a is the real droplet acceleration (or deceleration). Let us remind that a was measured by image analysis and its value can be found in Table II. Note also that gravity is much smaller than the measured acceleration. Second, the most amplified wavelength of Kelvin-Helmholtz instability is defined as

$$\lambda_{KH,max} = \frac{3\pi\sigma_L(\rho_D + \rho_A)}{U_+^2 \rho_D \rho_A} \tag{18}$$

Figure 12 shows a comparison between Rayleigh-Taylor and Kelvin-Helmholtz for the present experimental results (λ is obtained from image analysis). It can be seen on Figure 12, that for Weber numbers less than 60, no mechanism seems to be able to explain directly the observed wavelengths but for Weber numbers greater than 60, Kelvin-Helmholtz instabilities become good candidates to explain the observed waves for the higher Weber number observed. Anyhow, Rayleigh-Taylor instabilities can be ruled out experimentally and this seems in agreement with conclusions of section III C 2: momentum exchange and wake vortex prevent their appearance.

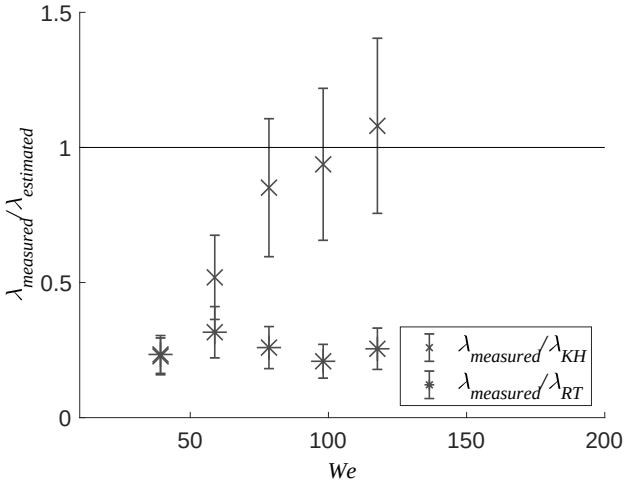

Figure 12: Wavelength of the measured and computed instability

D. Fragments Size

Larger droplets' PDF has been obtained by image analysis. Results can be seen on figure 13 for Weber numbers 59, 79 and 118 (for lower Weber numbers the number of fragments was not numerous enough to obtain smooth PDF). A log-normal law is fitted to the histograms as is usual in atomization studies[31] and as suggested by[46,47] and more recently[48].

$$f(x;\mu,\sigma) = \frac{1}{x\sigma\sqrt{2\pi}}\exp\left[-\frac{(\ln x - m_{50})^2}{2\sigma_{\ln d}^2}\right] \tag{19}$$

The log-normal distributions show a good fit with shift parameter $m_{50} = ln(d_{50\%})$ close to -2.2 meaning that the peak of daughter droplet is around one tenth of the initial droplet diameter and that 50% of the droplets are smaller (this is the definition of the median diameter $d_{50\%}$). The value of the scaling parameter $\sigma_{\ln d}$ of the distribution is also roughly constant and close to 0.8 showing that there is no real difference between Weber numbers 59 and 118. Moreover using a model for the turbulent re-agglomeration of ligaments by the surrounding fluid into drops[44] allows to compute the scale parameter $\sigma_{\ln d}$ of the log-normal law as

$$\sigma_{\ln d} = \frac{1}{2}\sigma_{\ln \varepsilon} \tag{20}$$

where $\sigma_{\ln \varepsilon}$ is the scale parameter of the log-stable law describing the intermittencies of turbulence[49]. In the latter paper, it was shown that

$$\sigma_{\ln \varepsilon}^{\alpha} = \ln\left(\frac{\lambda_T}{\eta}\right) \tag{21}$$

where $\alpha = 1.70$ is the stability parameter of the stable law, λ_T is the Taylor scale of turbulence and η is the Kolmogorov scale. In order to compute the ratio between these two values, it is possible to use the scaling law[50],

$$\frac{\lambda_T}{\eta} \propto Re^{\frac{1}{4}}. \tag{22}$$

This results in a very slowly varying function of Reynolds number and considering that Re ranges from 9765 to 13809

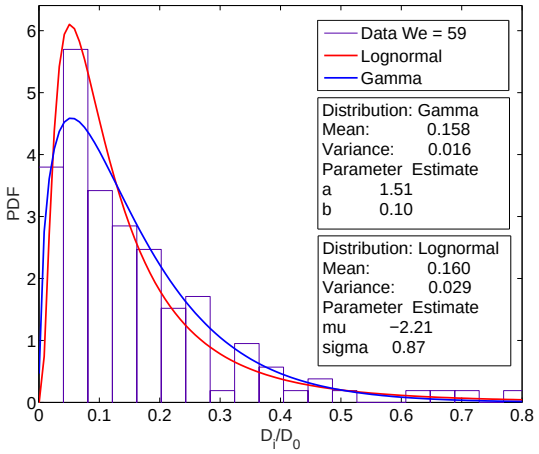

(a) We = 59

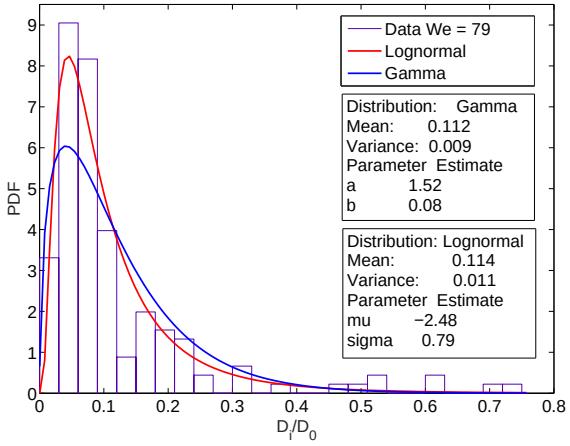

(b) We = 79

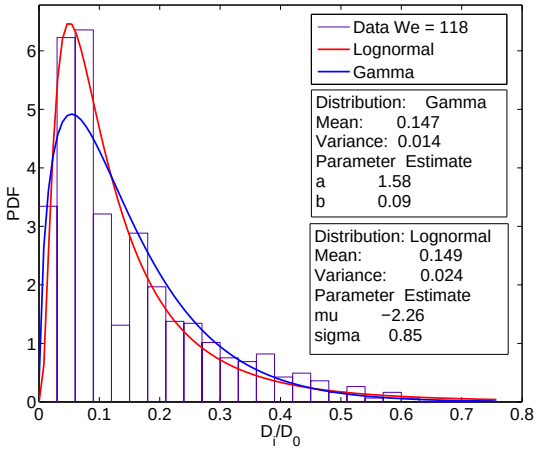

(c) We = 118

Figure 13: Droplet size distribution obtained by image analysis

leads to a value for $\sigma_{\ln d}$ close to 0.8 for all the Weber number considered, in agreement with our experimental results. Note that the initial model[49] considers log-stable laws with stability index 1.7, whereas log-normal laws are log-stable laws with stability index 2; it is impossible however in the present case to distinguish the two PDF as they mainly differ by the number of small droplets that the image analysis technique used cannot measure. The sieve analysis however shows an increase of small droplets that the log-normal law cannot describe (since its parameters are roughly constant between Weber numbers 59 and 118).

There is, however, some controversies concerning the use of log-normal distribution versus Gamma distribution[51,52]; moreover, recent studies[13] used Gamma distribution in the liquid-metal/water case. Therefore, for the sake of completeness, a comparison with the shape-scale formulation of the Gamma distribution (*cf.* equation 23, $a \approx 1.5$ in our fitting is the shape parameter and $b \approx 0.1$ is the scale parameter) is also shown on Figure 13.

$$f(x;a,b) = \frac{x^{a-1}e^{-\frac{x}{b}}}{b^a \Gamma(a)} \tag{23}$$

Up to the resolution of the PDF, it is very difficult to say which distribution prevails: concerning the number density function, the log-normal PDF seems to be slightly better but the Gamma distribution seems to describe better the large size part of the distribution and would therefore reproduce better the mass distribution of the particle. This could be related to the partial convergence of the image analysis based distribution as it is very long using this technique to get good converged results (for the lower Weber numbers there are therefore, for instance, some empty bins and this is difficult to assert directly whether this is physical or not). This may be another incentive to use the sieving technique. Note also on Figure 13 that gaps in the PDF located above $D_i/D_0 > 0.33$ can be identified as a separation between daughter droplets resulting either from the bag or from the rim breakup. This may also explain the slow convergence of rim droplets as few of them are produced and could explain the empty bin. Moreover, the ratio $D_i/D_0 \approx 0.8$ would correspond to a breakup of the droplet in two parts while $D_i/D_0 \approx 0.5$ corresponds to a breakup of the droplet in eight parts and $D_i/D_0 \approx 0.33$ in twenty-seven parts.

The data obtained after sieve analysis are shown in Appendix E in Table V. In our experiments, the Sauter Mean Diameter or SMD was calculated from the sieve mass distribution using the approximate formula

$$SMD \approx \frac{1}{\sum_{i=0}^{N_s} x_i/\bar{D}_i} \tag{24}$$

where x_i is the mass fraction of sieve number i and $\bar{D}_i = \frac{D_i+D_{i+1}}{2}$ an N_s the number of sieves used. Note that to compute $\bar{D}_i$, averaging is made with the immediately larger sieve in the set and that an extra "virtual" sieve has been added on top of the hierarchy corresponding to the size of the mother droplet, $D_0 \approx 4mm$. Uncertainty on the SMD is related to the range of sieve used and is therefore quite large in the present case (up to 50% if estimated by differentiating equation (24) and assuming that uncertainty on the droplet size is equal to half the bin

We	8	10	20	39	59	79	99	118
SMD/D_0	1	0.7248	0.7058	0.5230	0.4789	0.4344	0.4645	0.3615

Table IV: Experimental results for the ratio SMD/D_0.

size). Moreover, there exists another source of uncertainty as the sieving only selects the smallest length when the droplets are non spherical. This concerns mainly the biggest fragments however as the smaller ones are spherical. This introduces a systematic bias (toward the large scale as some "surface" is neglected). I can be suggested that its impact on the SMD is minimal as the surface generation is mainly carried by the small droplet. However, using the technique described in this paper it is difficult to precisely quantify this bias. Pictures of the fragments can be found in Appendix E.

Ratio between the measured SMD and the initial droplet radius D_0 are given on table IV. For Weber numbers around 10 and 20, the SMD/D_0 ratio is close to 0.7, meaning that on the average around three daughter droplets are produced which seems fairly realistic (*cf.* figure 7). A value close to $1/2$ is obtained in the $20 \leq We \leq 60$ range corresponding to around eight daughter droplets for a "mono-disperse equivalent" case.

E. Kinetic to surface energy balance

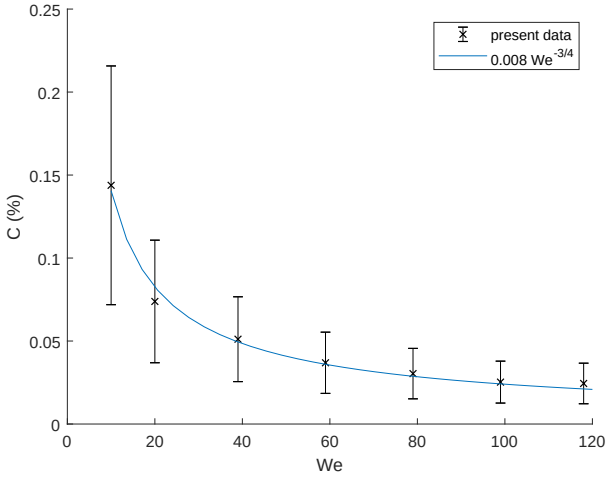

Figure 14: Kinetic energy ratio conversion to surface energy in present experiment.

To estimate the kinetic energy fraction converted to surface energy, C, the ratio of the total final surface energy after fragmentation S_f to the total initial kinetic energy $(1/2)m_t U_\infty^2$ of all droplets in the trial is computed,

$$C = \frac{S_f}{(1/2)m_t U_\infty^2} \tag{25}$$

$$S_f = \sum_{i=0}^{N_s} N_i^d A_i \sigma \tag{26}$$

where $N_i^d = m_i / \left(\frac{\pi}{6}\rho_D \bar{D}_i^{\,3}\right)$ is the approximate particles number for a given sieve diameter and A_i is the surface of the sphere with diameter $\bar{D}_i$, leading to the final formula:

$$C = \frac{1}{12}\frac{\rho_A}{\rho_D}\frac{D_0}{SMD}\frac{1}{We} \tag{27}$$

Figures 14 shows the kinetic energy fraction converted to surface energy. The ratio C decreases when the Weber number increases following a power law close to $We^{-3/4}$, with a small deviation for the larger Weber number that could hide an asymptotic value at large Weber numbers. It can be noted the very small value of this kinetic to surface energy transfer, showing that liquid fragmentation of single droplet is definitely not an efficient way of dividing matter.

IV. SCALING OF THE FRAGMENT SIZES WITH THE WEBER NUMBER BASED ON MASS AND ENERGY BALANCE

The goal of this section is to obtain a correlation for the fragment size that can be used in CFD codes. The present attempt will make use of a mass and energy balance in order to obtain a new correlation. This new correlation is very close to a power-law and allows for a possible interpretation of the different values of the characteristic Weber number already used in correlations for fragmentation by IRSN CFD codes for nuclear safety.

A. Mass and Energy Balance

This section is inspired from the work of Lee & Ryu[53] but with some adaptations, since they considered the continuous fragmentation of a jet. Here, only the initial and final conditions (before and after fragmentation) are considered. This circumvents the difficulties appearing when describing all the different stages and mechanisms studied in the preceding sections (bag formation, bag instability and breakup, ligaments behaviour...*etc.*) and their possible interactions; since the fragmentation mechanism is considered as a black-box compelled to obey to basic conservation laws (mass and energy). This leads to an empirical formula for the evolution of SMD with the Weber number that is not a power law but is quite similar. Neglecting the effect of gravity (*cf.* Appendix D), conservation equations of mass and energy for the droplet can be written as follows:

$$\rho_D \frac{\pi}{6} D_0^3 = \sum_{i=1}^{N_d} \rho_D \frac{\pi}{6} D_i^3 \tag{28}$$

$$\rho_D \frac{\pi}{12} D_0^3 U_\infty^2 + \sigma \pi D_0^2 = \sum_{i=1}^{N_d} \rho_D \frac{\pi}{12} D_i^3 U_i^2 + \sum_{i=1}^{N_d} \sigma \pi D_i^2 + \Phi \tag{29}$$

where Φ is the energy lost in the fragmentation process (either by viscous dissipation or transmitted to the surrounding fluid).

After some algebraic operations (*cf.* Appendix F), it can be shown that this leads to the relation,

$$\frac{SMD}{D_0} = \frac{We_c + 12\frac{\rho_A}{\rho_D}}{We(1-\phi') + 12\frac{\rho_A}{\rho_D}} \tag{30}$$

where $\phi' = 12\Phi/(\rho_D \pi D_0^3 U_\infty^2)$ is the dimensionless energy loss (*i.e.* the energy loss divided by the initial kinetic energy of the droplet) and We_c a characteristic Weber number (*i.e.* the characteristic Weber number of the daughter droplets).

In order to determine the value of this characteristic Weber number, an explanation can be found in[33,35,54], where a threshold of 3.27 is obtained thanks to potential flow analysis on spheroidal bubbles and droplets. Note that this is very different from the value of 12 usually assumed as a limit for the bag breakup. Rimbert *et al.*[35] gives some reasons for the existence of this second threshold actually closer to 13.

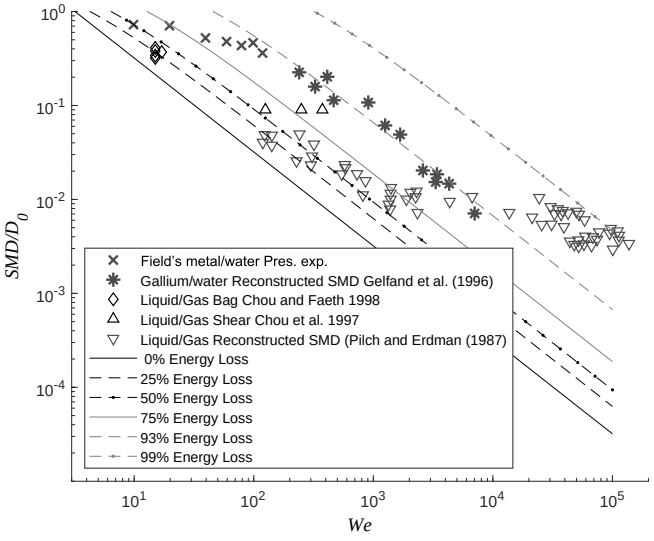

Figure 15: Secondary fragmentation model. Non dimensional SMD as a function of the Weber number. Iso-lines stand for a given energy loss. Dark symbols are for liquid-liquid cases and open symbols are for gas-liquid cases. Lines of iso-energy loss are depicted.

Figure 15 shows a comparison between the present experimental results and others[6] for high Weber numbers and the present model (represented by lines of equal energy loss). In the present experiments, the energy loss seems to be increasing from 50% to a limiting value close to 90%. This means that, for the higher Weber numbers, the droplet retains only 10% of their initial energy. Since surface energy can be neglected (*cf.* section III E), these remaining 10% can be assumed to be residual kinetic energy.

Figure 15 also depicts some previous results[6] for liquid-liquid system and for liquid-air systems[1,37]. Note that very high Weber numbers are difficult to reach in present experiments while old measurements[6] used entirely different systems generating underwater shock waves to obtain high Weber numbers. In many of these old review papers, thought the data are referred as average fragment size, it is sometime unclear which "average" diameter has been used. It is quite likely that it was the Mass Median Diameter as it was current at that time and not the Sauter Mean Diameter as it is considered here. Therefore, to convert this MMD into a proper SMD it has been assumed that the MMD/SMD ratio is equal to 1.2 as reported in many works[32,37,55,56]. This is somehow arbitrary however and it only emphasizes the need for new data in the high Weber number range. However using this conversion factor we can notice the continuity of present and former liquid-liquid results[6]. But, as previously emphasized, the data found in theses review papers are quite ancient and using them directly, without introducing a MMD/SMD ratio, would have led to a much higher energy loss.

Lastly, assuming the same proportionality ratio between MMD and SMD, a comparison is made with gas-liquid results collected in review[1]. It can then be observed that the energy loss tremendously increases in this regime reaching 99% for the higher Weber numbers. An explanation of this slowdown of the fragmentation can be found in the viscous boundary layer dominated mechanism of production of droplet proposed by Hsiang & Faeth[34]. In the shear breakup mode, they have found that

$$\frac{SMD}{D_0} = C_s \left(\frac{\rho_D}{\rho_A}\right)^{\frac{1}{4}} \left(\frac{\nu_L}{U_\infty D_0}\right)^{\frac{1}{2}} \tag{31}$$

with constant C_s equals to 6.2. Therefore in this model, the size of drops only depends on the liquid Reynolds number; using present (Oh, We) notation, this turns to

$$\frac{SMD}{D_0} = C_s Oh^{\frac{1}{2}} We^{-\frac{1}{4}} \tag{32}$$

and this scaling is displayed on figure (16). To obtain equation (32), Hsiang & Faeth[34] used a simple model for the development of the boundary layer inside the drop and assume that the SMD is proportional to the thickness of the boundary layer. In this model, atomization is a purely viscous phenomenon and surface tension does not govern the size of the resulting drops. Using a dimensionless Weber number based on the SMD, they[34] found their correlation to be valid in all atomization regimes. In the present case, it can be seen on figure 16, that this law seems to describe the high-Weber data range of Pilch and Erdman when C_s is close to 1.5. (Some caution must be made here as most of these data[1] comes from reports[57,58] and

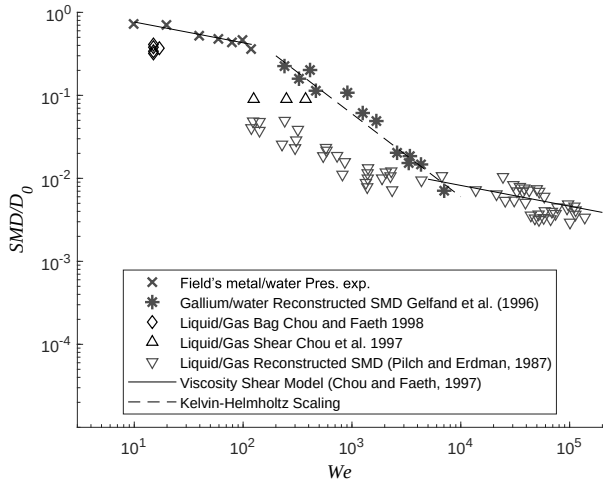

Figure 16: Dimensionless SMD as function of We number. Dark symbols are for liquid-liquid cases and open symbols are for gas-liquid cases. Correlations based on power law analysis are depicted.

only one journal paper[59] and involves water droplets ranging from 0.5 to 5.0 mm diameter, therefore the Ohnesorge numbers range from 1.6×10^{-3} to 5×10^{-3}. A middle value of 3×10^{-3} has been used here to fix the constant C_s.) It can also be seen that law seems valid for the present low Weber number data set but with $C_s\approx485$ which suggests that another mechanism should be actually at work. More interestingly, this concurs with equation (27) and the scaling $C\propto We^{-3/4}$. Similarly, one can get for Kelvin-Helmholtz waves[45], a scaling

$$\frac{\lambda_{KH,max}}{D_0}=\frac{3\pi(\rho_D+\rho_A)}{\rho_D}\frac{1}{We}\propto We^{-1} \tag{33}$$

and it is therefore often assumed that the SMD/D_0 ratio of droplets generated by Kelvin-Helmholtz wave should scale like We^{-1}. This scaling is also depicted on figure 16. This is an interial regime and it also means that the kinetic to surface energy ratio given by equation (27) becomes constant as was found by Lhuissier *et al.*[60]. The average number of daughter droplets then scales as $N_d\propto(D_0/SMD)^3\propto We^3$, as also found by Lhuissier *et al.*[60]. In the present low Weber number range, the scaling becomes $N_d\propto(D_0/SMD)^3\propto We^{3/4}$.

B. Gas-Liquid and Liquid-Liquid Limit Cases

In the limiting gas-liquid case where $\rho_D/\rho_A\gg1$, equation (30) is very similar to a power law with exponent -1 when the energy loss ϕ' is constant.

$$\frac{SMD}{D_0}\approx\frac{We_c}{(1-\phi')}\frac{1}{We} \tag{34}$$

It is therefore possible to introduce an effective characteristic Weber number $We_{c,eff}$ such as

$$We_{c,eff}=\frac{We_c}{(1-\phi')} \tag{35}$$

The limiting Weber number We_c has been shown to be equal to 3.27 by considering potential flow around a spheroid. Considering the gas-liquid case and $\phi'=50\%$ (*cf.* figure 15), the effective Weber number $We_{c,eff}$ becomes 6.5 which is in agreement with observations[3,4] for the beginning of the fragmentation threshold in the gas-liquid case.

In the liquid-liquid case, when $\rho_D/\rho_A\approx1$, equation (30) does not reduce to a simple power law and ϕ' increases from 50 % to 90%. Considering, for instance, the case where $\rho_D/\rho_A=8$ and $\phi'=75\%$, equation (30) becomes

$$\frac{SMD}{D_0}\approx\frac{18}{We+6}\approx\frac{18}{We} \tag{36}$$

for large Weber numbers. So there is still an effective characteristic Weber number $We_{c,eff}=18$ (if $\phi'=90\%$ then $We_{c,eff}=45$) but it does not represent the beginning of the fragmentation regime but rather the characteristic size (SMD) of the fragments. For the beginning of fragmentation, let us assume that $\phi'=25\%$ and equation (30) becomes

$$\frac{SMD}{D_0}\approx\frac{18}{3We+6} \tag{37}$$

So that the limit is given when $SMD/D_0=1$ by $We=4$, closer to the value of 3.27. In present experiments, the higher value of 8 can be partly explained by the velocity decrease (jump) when the droplet crosses the interface, since this results in a corrected Weber number $We^*\approx4.7$.

These considerations are of particular interest for the fragmentation modelling in nuclear safety oriented code such as MC3D[16,17] where different characteristic Weber numbers are usually used for computing the SMD of the fragments in the liquid-liquid and the gas-liquid case[61].

V. CONCLUSIONS

In this paper, we experimentally investigated the breakup in water pool of a metallic droplet at low Weber numbers with an emphasis on bag breakup. By controlling the pool temperature we were able to inhibit the influence of solidification on the fragmentation mechanism while allowing daughter droplets to freeze before hitting the bottom of the pool.

It was shown that the droplet velocity quickly change after crossing the interface. Moreover, fragmentation steps for the bag breakup regime in a liquid-liquid system are similar to those observed for a gas-liquid system. However the orientation of the bag was not the same as in liquid-gas systems which led us to consider another deformation mechanism due to strong wake vortex interaction. The sheet thereafter seems to destabilize mainly thanks to Kelvin-Helmholtz instability and Rayleigh-Taylor instability seems to be absent whereas it

is usually thought to be dominant in the gas-liquid case. Image analysis of the fragments has shown that they exhibit a log-normal size Number Density Function (valid for the large fragments) and that its width can be computed thanks to a turbulent re-agglomeration mechanism of the ligaments. A sieve analysis of the solidified fragments has been performed, leading to their mass distribution. Both the number and mass of smaller fragments increase when the Weber number increases. Therefore the dependency of the Sauter Mean Diameter on the Weber number was investigated and actually showed a decrease of SMD when the Weber number increases. Lastly, an energy balance between the initial and final kinetic and surface energy has been performed. Experimentally it has been shown that a negligible amount of the initial kinetic energy can be converted into surface energy during fragmentation. From present modeling, it has been estimated that from 75% to 90 % of the initial kinetic energy has been lost to the surrounding fluid by the droplet during the fragmentation process and it therefore retain only from 10% to 25% of its initial kinetic energy. However when $We > 4000$, comparison with review data[1] shows that in the Boundary Layer Stripping regime, energy loss by the droplet increases tremendously reaching up to 99%.

To conclude, all these considerations have to be moderated considering that present data and, to a greater extent, previously published data are still relatively imprecise. This will lead us to develop new methods to compute the SMD using a larger number of sieves. This should allow for a more precise determination of the energy loss and is left for future work. Meanwhile, the present facility should be overhauled to allow for larger Weber number experiments.

Moreover, on the theoretical side, a model for the energy loss is needed and shall be developed; the vortex ring generation seems an interesting lead but the interplay between the different phenomena (initial deformation, wake vortex, sheet instability, sheet rupture, influence of turbulent structures on the breakup/re-agglomeration of ligaments) makes it a challenging task.

Lastly, interplay between solidification and fragmentation has to be more thoroughly investigated.

VI. ACKNOWLEDGEMENTS

The work was done under the research program on nuclear safety and radioprotection (RSNR) and received funding from French government managed by the National Research Agency (ANR) under Future Investments Program (PIA), research grant No: ANR-10-RSNR-01.

The authors also acknowledge partial support from COST action MP1305 "Flowing Matter", supported by COST (European Cooperation in Science and Technology)".

Lastly, the authors would also like to thank our colleagues at LEMTA, Dr. Yvan Dossman, for helpful comments and careful reading of this manuscript, Dr. Yves Jannot for kindly performing the ADS analysis of the Field's metal and Dr. Salahedine Skali-Lamy, Dr. Sebastien Kiesgen de Richter and Dr. Denis Funfschilling (now from ICube) for their help in determing Field's metal viscosity.

VII. AUTHOR DECLARATION

A. Conflict of intest

The authors have no conflicts to disclose.

VIII. DATA AVAILABILITY

The data that supports the findings of this study are available within the article.

Appendix A: Initial Weber Number for a Spheroidal Droplet

The surface of a prolate spheroid is given by equation (A1).

$$A = 2\pi\left(b^2 + \frac{ab}{e}\mathrm{Arcsin}\,(e)\right) \tag{A1}$$

where a is the greater semi-axis and b is the lesser semi-axis and e is the eccentricity given by equation (A2)

$$e = \frac{\sqrt{a^2-b^2}}{a} \tag{A2}$$

Starting from this it is possible to write the classical Weber number as

$$We = 12\frac{\mathrm{Kinetic\_energy}}{\mathrm{Surface\_energy}} \tag{A3}$$

because for a spherical droplet, equality between kinetic and surface energy is obtained for $We = 12$. A rather straightforward computation then show that far a droplet initially in a spheroidal shape, introducing the deformation parameter $\chi = a/b$, the Weber number reads

$$We(\chi) = F(\chi)We \tag{A4}$$

where We is the Weber number for the spherical droplet of equivalent volume and correction function F reads

$$F\,(\chi) = \frac{\chi^{2/3}}{6\left(1+\frac{\chi\mathrm{Arcsin}\sqrt{1-1/\chi^2}}{\sqrt{1-1/\chi^2}}\right)} \tag{A5}$$

Figure 17 shows the behaviour of function F. Since $F(2.04) \approx 0.925$, this yields a 7% underestimation of the initial Weber number.

Appendix B: Surface Tension Measurement

Surface Tension is obtained from[22]

$$\gamma = \Delta\rho g R_0^2/\beta \tag{B1}$$

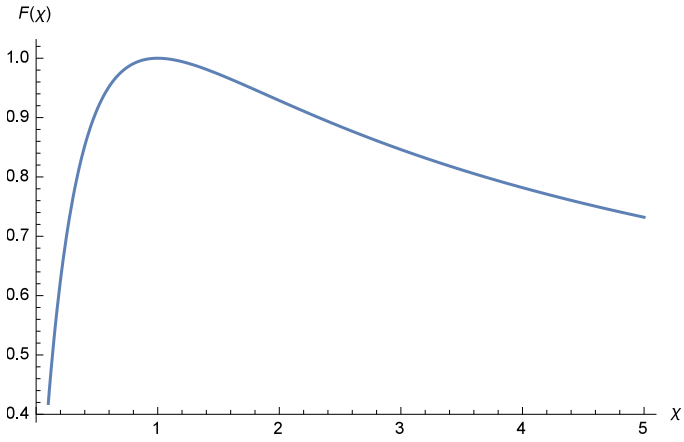

Figure 17: Correction function F

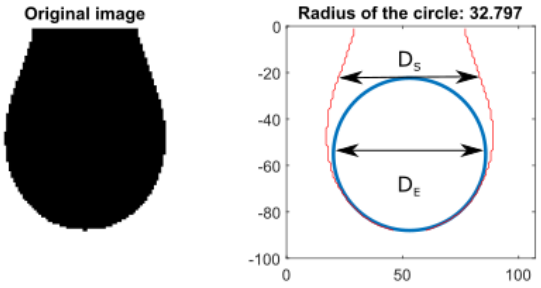

Figure 18: Surface tension measurement. The nozzle radius us 48 pixels wide (for 2 mm)

where

$$\beta = 0.12836 - 0.7577\frac{D_S}{D_E} + 1.7713\left(\frac{D_S}{D_E}\right)^2 - 0.5426\left(\frac{D_S}{D_E}\right)^3 \tag{B2}$$

is obtained from image analysis (*cf.* figure 18). D_E is the diameter of the osculating circle to the drop bottom and D_S is the length of the segment tangent to this circle on the top.

Appendix C: Velocity Jump Modelling

Using the unsteady Bernoulli relationship between the two liquid phases leads to

$$\rho_A \frac{\partial \Psi_A}{\partial t} + \frac{1}{2}\rho_A U_A^2 = \rho_D \frac{\partial \Psi_D}{\partial t} + \frac{1}{2}\rho_D U_D^2. \tag{C1}$$

Using Ranger and Nicholls characteristic time,

$$\frac{\partial \Psi_A}{\partial t} \approx \frac{2R_0 U_A}{\tau_{RN}} \tag{C2}$$

$$\frac{\partial \Psi_D}{\partial t} \approx \frac{2R_0 U_D}{\tau_{RN}} \tag{C3}$$

yields

$$\frac{\partial \Psi_A}{\partial t} \approx \frac{2R_0 U_A}{\frac{2R_0}{U_A}\sqrt{\frac{\rho_D}{\rho_A}}} = \left(\frac{\rho_A}{\rho_D}\right)^{1/2} U_A^2 \tag{C4}$$

and

$$\frac{\partial \Psi_D}{\partial t} \approx \frac{2R_0 U_D}{\frac{2R_0}{U_A}\sqrt{\frac{\rho_D}{\rho_A}}} = \left(\frac{\rho_A}{\rho_D}\right)^{1/2} U_D U_A. \tag{C5}$$

Equation (C1) now reads

$$\left(\left(\frac{\rho_A}{\rho_D}\right)^{1/2} + \frac{1}{2}\right)\rho_A U_A^2 = \rho_D U_D^2 \left[\frac{1}{2} + \left(\frac{\rho_A}{\rho_D}\right)^{1/2}\frac{U_A}{U_D}\right] \tag{C6}$$

Setting x as the velocity ratio between the carrier phase and the liquid metal and using the density ratio ρ_R

$$x = \frac{U_A}{U_D} \tag{C7}$$

Equation (C5) turns to

$$\frac{x^2}{\rho_R^{-1/2}x + \frac{1}{2}} = \frac{\rho_R}{\rho_R^{-1/2} + \frac{1}{2}}. \tag{C8}$$

After resolution of the second order equation and setting $y = 1/x$ as the ratio, $\frac{U_D}{U_A}$, that matters, one gets

$$y = \frac{\rho_R^{-1} + 2\rho_R^{-3/2}}{\rho_R^{-1/2} \pm \sqrt{2(\rho_R^{-1} + \rho_R^{-3/2})}} \sim_\infty \rho_R^{-3/4} \tag{C9}$$

Value of the velocity jump for $\rho_R = 8$ is of the order of magnitude 0.23 very close to the experimental value of 0.26. Note that using the steady Bernoulli equation would have led to a ratio of $\rho_R^{-1/2} = 0.35$.

Appendix D: Influence of gravity

Average displacement of the droplet during breakup can be estimated to be close to

$$\Delta h = U t_{RN} \approx \sqrt{\frac{\rho_D}{\rho_A}} D \tag{D1}$$

The variation of gravity potential energy possessed by the droplet is negligible if

$$\frac{1}{2}\rho_D U^2 \gg \Delta\rho g \Delta h \tag{D2}$$

Then introducing the Bond number $Bo = \Delta\rho g D^2/\sigma$, the effect of gravity is negligible when

$$We \gg 2\sqrt{\frac{\rho_D}{\rho_A}} Bo \tag{D3}$$

In the present case $Bo = 1.26$ so that $We \gg 7$, or more rigorously 21 if we assume breakup occurs when $t_{br} \approx 3t_{RN}$. Therefore, it can be assumed that gravity has few effects during the breakup of the drop but does affect the oscillating modes (oblate and prolate).

Appendix E: Mass Measurements

Figure19 shows the fragments as obtained after sieving. While the smaller fragments are spherical, the larger ones may not be. This clearly induces a bias as the sieving techniques collect particles from their smallest Feret diameter (due to the agitation of the sieves). As far as SMD is concerned, this bias has been neglected as surface area is mainly the result of the smallest particles.

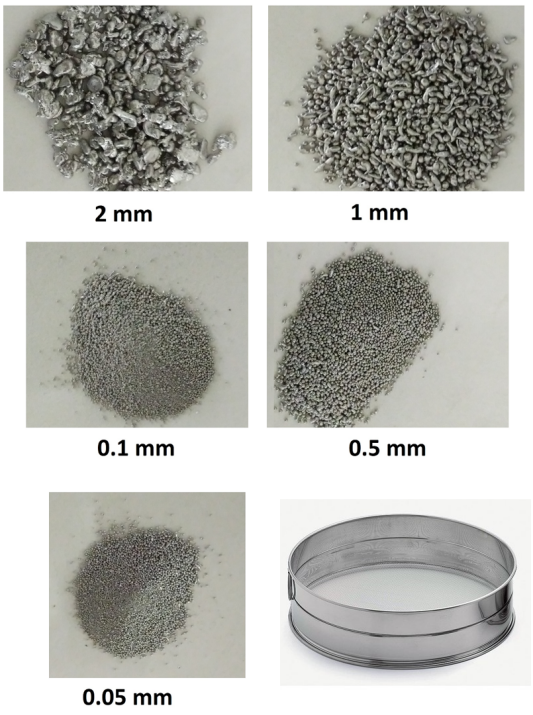

Figure 19: Picture of the fragments classification obtained by the sieving technique.

Table V collects the measurement that have been made using the sieving technique.

Appendix F: Balance of Mass and Energy, Calculus Details

If we assume a large number of daughter droplets described by a size-velocity PDF $P(D,U)$ and a marginal size PDF $P(D)$, the sum over the daughter droplets can be replaced by a sum weighted by the PDF (this is an ergodic hypothesis; let us recall that over 200 experiments are averaged). and the equations (28) and (29) can be written as follow,

$$\rho_D \frac{\pi}{6} D_0^3 \simeq \int_0^{D_{max}} N_d \rho_D \frac{\pi}{6} D^3 p(D)\,\mathrm{d}D \tag{F1}$$

where N_d is the total number of droplets.

$$\sigma\pi D_0^2 + \rho_D \frac{\pi}{6} D_0^3 \frac{U_\infty^2}{2} \simeq \int_0^{D_{max}} \int_0^{U_{max}} N_d \rho_D \frac{\pi}{12} D^3 U^2 p(D,U)\mathrm{d}D\mathrm{d}U + \int_0^{D_{max}} N_d \sigma\pi D^2 p(D)\,\mathrm{d}D + \Phi \tag{F2}$$

The next step is to write equations (28) and (29) in terms of size class obtained from the sieve analysis. For the equations (28), we have,

$$\rho_D \frac{\pi}{6} D_0^3 = \int_0^{D_{max}} N_d \rho_D \frac{\pi}{6} D^3 p(D)\mathrm{d}D \simeq N_d \sum_{i=1}^{N_c} \rho_D \frac{\pi}{6} D_i^3 p(D_i)\Delta D_i \tag{F3}$$

As can be seen, now the sum is done by using the number of classes N_c instead of the droplet number N_d. For the surface energy:

$$\sum_{i=1}^{N_d} \sigma\pi D_i^2 = \int_0^{D_{max}} N_d \sigma\pi D^2 p(D)\mathrm{d}D = N_d \sigma\pi \sum_{i=1}^{N_c} D_i^2 p(D_i)\Delta D_i \tag{F4}$$

For the equations (F2) using the definition of the marginal distribution, we can rewrite the third term of the kinetic energy as follow,

$$\sum_{i=1}^{N_d} \rho_D \frac{\pi}{12} D_i^3 U_i^2 = \int_0^{D_{max}} \int_0^{U_{max}} N_d \rho_D \frac{\pi}{12} U^2 D^3 p(D,U)\mathrm{d}D\mathrm{d}U = N_d \sum_{i=1}^{N_c} \rho_D \frac{\pi}{12} D_i^3 \int_0^{U_{max}} U^2 p(D_i,U)\,\Delta D_i \mathrm{d}U \tag{F5}$$

By integrating the second term with respect to the variable U, we can define the mean square velocity,

$$\int_0^{U_{max}} U^2 p(D_i,U)\,\Delta D_i \mathrm{d}U = \overline{U^2(D_i)} p(D_i)\Delta D_i \tag{F6}$$

This leads us to this relation,

$$\sum_{i=1}^{N_d} \rho_D \frac{\pi}{12} D_i^3 U_i^2 = N_d \sum_{i=1}^{N_c} \rho_D \frac{\pi}{12} D_i^3 \overline{U^2(D_i)} p(D_i)\Delta D_i \tag{F7}$$

If we rewrite equations (29), we have,

$$\sigma\pi D_0^2 + \rho_D \frac{\pi}{12} D_0^3 U_\infty^2 = N_d \sum_{i=0}^{N_c} \rho_D \frac{\pi}{12} D_i^3 \overline{U^2(D_i)} p(D_i)\Delta D_i + N_d \sum_{i=0}^{N_c} \sigma\pi D_i^2 p(D_i)\Delta D_i + \Phi \tag{F8}$$

We can then divide all the terms of equation (F7) by the initial kinetic energy, to make then the Weber number appear,

$$\frac{\rho_A}{\rho_D} \frac{12}{We_0} + 1 = N_d \sum_{i=0}^{N_c} \frac{We_i}{We_0} \frac{D_i^2}{D_0^2} p(D_i)\Delta D_i + N_d \sum_{i=0}^{N_c} \frac{\rho_A}{\rho_D} \frac{12}{We_0} \frac{D_i^2}{D_0^2} p(D_i)\Delta D_i + \Phi' \tag{F9}$$

D_i	20 µm	50 µm	100 µm	500 µm	1000 µm	2000 µm	Total Mass
$We = 118$	0 g	0.018 g	1.069 g	6.219 g	24.816 g	17.937 g	50.058 g
$We = 99$	0 g	0.012 g	1.243 g	5.264 g	23.933 g	33.874 g	64.326 g
$We = 79$	0 g	0.008 g	1.235 g	5.187 g	20.150 g	38.314 g	64.894 g
$We = 59$	0 g	0.000 g	0.230 g	5.543 g	13.775 g	43.511 g	61.000 g
$We = 39$	0 g	0.000 g	0.226 g	3.483 g	13.539 g	42.708 g	59.952 g
$We = 20$	0 g	0.000 g	0.0118 g	0.340 g	2.630 g	57.069 g	60.050 g
$We = 10$	0 g	0.000 g	0.130 g	0.1059 g	0.4885 g	59.623 g	60.231 g

Table V: Mass measurements by sieving. Note that the 100 µm sieve corresponds approximately to the resolution of the high-speed camera

where $We_i = \rho_A \overline{U^2(D_i)} D_i/\sigma$ and $\phi' = 12\Phi/(\rho_D \pi D_0^3 U_\infty^2)$ is the ratio of the dissipated kinetic energy to the initial kinetic energy. We can then rewrite the third term as follows:

$$\begin{aligned} \sum_{i=0}^{N_c} We_i \frac{D_i^2}{D_0^2} p(D_i)\Delta D_i &\approx \int_0^{D_{max}} We(D) \frac{D^2}{D_0^2} p(D)\,\mathrm{d}D \\ &= We(D_c) \int_0^{D_{max}} \frac{D^2}{D_0^2} p(D)\,\mathrm{d}D \end{aligned}, \quad \text{(F10)}$$

by using the first mean value theorem for integrals, where $D_c \in [0, D_{max}]$ and $We_c = We(D_c)$. We_c can be considered as a parameter variable representing the mean value of the final Weber number. To conclude, we can then express N_d from the equation (F3),

$$N_d = \frac{D_0^3}{\sum_{i=0}^{N_c} D_i^3 p(D_i)\Delta D_i} \quad \text{(F11)}$$

Let us recall that Sauter Mean Diameter or SMD is also written D_{32} as it is defined from the discrete Number Density Function as:

$$SMD = D_{32} = \frac{\sum_{i=0}^{N_c} D_i^3 p(D_i)\Delta D_i}{\sum_{i=0}^{N_c} D_i^2 p(D_i)\Delta D_i}. \quad \text{(F12)}$$

By replacing N_d in equations (F9) by equation (F11) and using Equations (F10) and (F12), we obtain,

$$12\frac{\rho_A}{\rho_D} + We_0 = \left(We_c + 12\frac{\rho_A}{\rho_D}\right)\frac{D_0}{SMD} + \phi' We_0 \quad \text{(F13)}$$

which leads to the desired result.

REFERENCES

[1] M. Pilch and C. Erdman, "Use of breakup time data and velocity history data to predict the maximum size of stable fragments for acceleration-induced breakup of a liquid drop," International Journal of Multiphase Flow **13**, 741–757 (1987).

[2] L.-P. Hsiang and G. Faeth, "Drop deformation and breakup due to shock wave and steady disturbances," International Journal of Multiphase Flow **21**, 545–560 (1995).

[3] T. G. Theofanous, G. J. Li, and T. N. Dinh, "Aerobreakup in Rarefied Supersonic Gas Flows," Journal of Fluids Engineering **126**, 516 (2004).

[4] E. Villermaux and B. Bossa, "Single-drop fragmentation determines size distribution of raindrops," Nature Physics **5**, 697–702 (2009).

[5] T. Theofanous, "Aerobreakup of Newtonian and Viscoelastic Liquids," Annual Review of Fluid Mechanics **43**, 661–690 (2011).

[6] B. Gelfand, "Droplet breakup phenomena in flows with velocity lag," Progress in Energy and Combustion Science **22**, 201–265 (1996).

[7] D. Guildenbecher, C. López-Rivera, and P. Sojka, "Secondary atomization," Experiments in Fluids **46**, 371 (2009).

[8] S. A. Krzeczkowski, "Measurement of liquid droplet disintegration mechanisms," International Journal of Multiphase Flow **6**, 227–239 (1980).

[9] A. Flock, D. Guildenbecher, J. Chen, P. Sojka, and H.-J. Bauer, "Experimental statistics of droplet trajectory and air flow during aerodynamic fragmentation of liquid drops," International Journal of Multiphase Flow **47**, 37–49 (2012).

[10] P. D. Patel and T. G. Theofanous, "Hydrodynamic fragmentation of drops," Journal of Fluid Mechanics **103**, 207–223 (1981).

[11] D. Kim, M. Burger, G. Frohlich, and H. Unger, "Experimental investigation of hydrodynamic fragmentation of gallium drops in water flows Chapter 6," in *Proceedings of the international meeting on light water severe accident evaluation*, edited by American Nuclear Society (Stone & Webster Engineering Corp, 1983).

[12] J.-W. Yang and H.-S. Yang, "Liquid-liquid mixing for the breakup of accelerating drops," Korean Journal of Chemical Engineering **7**, 22–30 (1990).

[13] J.-B. Wacheul, M. Le Bars, J. Monteux, and J. M. Aurnou, "Laboratory experiments on the breakup of liquid metal diapirs," *Earth and Planetary Science Letters*, **403**, 236–245 (2014).

[14] M. Landeau, R. Deguen, and P. Olson, "Experiments on the fragmentation of a buoyant liquid volume in another liquid," Journal of Fluid Mechanics **749**, 478–518 (2014).

[15] B. R. Morton, G. Taylor, and J. S. Turner, "Turbulent Gravitational Convection from Maintained and Instantaneous Sources," Proceedings of the Royal Society A: Mathematical, Physical and Engineering Sciences **234**, 1–23 (1956).

[16] R. Meignen, S. Picchi, J. Lamome, B. Raverdy, S. C. Escobar, and G. Nicaise, "The challenge of modeling fuel–coolant interaction: Part I – Premixing," Nuclear Engineering and Design **280**, 511–527 (2014).

[17] R. Meignen, B. Raverdy, S. Picchi, and J. Lamome, "The challenge of modeling fuel–coolant interaction: Part II – Steam explosion," Nuclear Engineering and Design (2014), 10.1016/j.nucengdes.2014.08.028.

[18] M. Jeyakumar, M. Hamed, and S. Shankar, "Rheology of liquid metals and alloys," Journal of Non-Newtonian Fluid Mechanics **166**, 831–838 (2011).

[19] Q. Xu, N. Oudalov, Q. Guo, H. M. Jaeger, and E. Brown, "Effect of oxidation on the mechanical properties of liquid gallium and eutectic gallium-indium," Physics of Fluids **24**, 063101 (2012).

[20] L.-H. Luu and Y. Forterre, "Drop impact of yield-stress fluids," Journal of Fluid Mechanics **632**, 301 (2009).

[21] Y. Rotenberg, L. Boruvka, and A. Neumann, "Determination of surface tension and contact angle from the shapes of axisymmetric fluid interfaces," Journal of colloid and interface science **93**, 169–183 (1983).

[22] F. Hansen and G. Rødsrud, "Surface tension by pendant drop: I. a fast standard instrument using computer image analysis," Journal of colloid and interface science **141**, 1–9 (1991).

[23] I. Egry, E. Ricci, R. Novakovic, and S. Ozawa, "Surface tension of liquid metals and alloys—recent developments," Advances in colloid and interface science **159**, 198–212 (2010).

[24] X. Zhao, S. Xu, and J. Liu, "Surface tension of liquid metal: role, mechanism and application," Frontiers in Energy **11**, 535–567 (2017).

[25]N. Kouraytem, E. Li, and S. T. Thoroddsen, "Formation of microbeads during vapor explosions of field's metal in water," Physical Review E **93**, 063108 (2016).
[26]Y. Jannot, Z. Acem, and A. Kanmogne, "Transient hot plate method with two temperature measurements for thermal characterization of metals," Measurement Science and Technology **17**, 69–74 (2006).
[27]A. Lipchitz, G. Harvel, and T. Sunagawa, "Experimental investigation of the thermal conductivity and viscosity of liquid in-bi-sn eutectic alloy (field's metal) for use in a natural circulation experimental loop," in *Proceedings of the 23th International Conference on Nuclear Engineering (ICONE-23),(Japan Society of Mechanical Engineers, 2015)* (2015) p. 3737.
[28]A. Amirzadeh, M. Raessi, and S. Chandra, "Producing molten metal droplets smaller than the nozzle diameter using a pneumatic drop-on-demand generator," Experimental Thermal and Fluid Science **47**, 26–33 (2013).
[29]A. A. Ranger and J. Nicholls, "Aerodynamic shattering of liquid drops." AIAA Journal **7**, 285–290 (1969).
[30]M. A. Weiss and C. H. Worsham, "Atomization in high velocity airstreams," ARS Journal **29**, 252–259 (1959).
[31]Arthur Lefebvre, *Atomization and Sprays* (Taylor & Francis, 1988).
[32]W.-H. Chou, L.-P. Hsiang, and G. Faeth, "Temporal properties of drop breakup in the shear breakup regime," International Journal of Multiphase Flow **23**, 651–669 (1997).
[33]D. Moore, "The rise of a gas bubble in a viscous liquid," Journal of Fluid Mechanics **6**, 113–130 (1959).
[34]L. P. Hsiang and G. M. Faeth, "Near-limit drop deformation and secondary breakup," International Journal of Multiphase Flow **18**, 635–652 (1992).
[35]N. Rimbert, S. Castrillon Escobar, R. Meignen, M. Hadj-Achour, and M. Gradeck, "Spheroidal droplet deformation, oscillation and breakup in uniform outer flow," Journal of Fluid Mechanics **904**, A15 (2020).
[36]G. K. Batchelor, "An Introduction to Fluid Dynamics," (1967).
[37]W.-H. Chou and G. Faeth, "Temporal properties of secondary drop breakup in the bag breakup regime," International Journal of Multiphase Flow **24**, 889–912 (1998).
[38]L. Opfer, I. V. Roisman, J. Venzmer, M. Klostermann, and C. Tropea, "Droplet-air collision dynamics: Evolution of the film thickness," Physical Review E **89**, 013023 (2014).
[39]N. Baumann, D. D. Joseph, P. Mohr, and Y. Renardy, "Vortex rings of one fluid in another in free fall," Physics of Fluids A: Fluid Dynamics **4**, 567 (1992).
[40]B. Peck and L. Sigurdson, "The three-dimensional vortex structure of an impacting water drop," Physics of Fluids **6**, 564 (1994).
[41]E. Y. Harper, G. W. Grube, and I.-D. Chang, "On the breakup of accelerating liquid drops," Journal of Fluid Mechanics **52**, 565–591 (1972).
[42]D. D. Joseph, G. S. Beavers, and T. Funada, "Rayleigh–Taylor instability of viscoelastic drops at high Weber numbers," Journal of Fluid Mechanics **453** (2002), 10.1017/S0022112001006802.
[43]H. Zhao, H.-F. Liu, W.-F. Li, and J.-L. Xu, "Morphological classification of low viscosity drop bag breakup in a continuous air jet stream," Physics of Fluids **22**, 114103 (2010).
[44]N. Rimbert and G. Castanet, "Crossover between Rayleigh-Taylor instability and turbulent cascading atomization mechanism in the bag-breakup regime." Physical review. E, Statistical, nonlinear, and soft matter physics **84**, 016318 (2011).
[45]Y. Abe, T. Kizu, T. Arai, H. Nariai, K. Chitose, and K. Koyama, "Study on thermal-hydraulic behavior during molten material and coolant interaction," Nuclear Engineering and Design **230**, 277–291 (2004).
[46]A. N. Kolmogorov, "On the lognormal distribution law of the dimensions of particles under pulverization," in *Doklady of the Akademy of Sciences of the USSR*, Vol. 31 (1941) pp. 99–101.
[47]M. A. Gorokhovski and V. L. Saveliev, "Analyses of Kolmogorov's model of breakup and its application into Lagrangian computation of liquid sprays under air-blast atomization," Physics of Fluids **15**, 184–192 (2003).
[48]M. Jain, R. S. Prakash, G. Tomar, and R. V. Ravikrishna, "Secondary breakup of a drop at moderate Weber numbers," Proceedings of the Royal Society A: Mathematical, Physical and Engineering Sciences **471**, 20140930–20140930 (2015).
[49]N. Rimbert, "Simple model for turbulence intermittencies based on self-avoiding random vortex stretching," Physical Review E - Statistical, Nonlinear, and Soft Matter Physics **81** (2010), 10.1103/PhysRevE.81.056315.
[50]H. Tennekes and J. L. Lumley, *A First Course in Turbulence* (MIT Press, 1972) p. 300.
[51]P. Marmottant and E. Villermaux, "On spray formation," Journal of fluid mechanics **498**, 73–111 (2004).
[52]D. Lamb and J. Verlinde, *Physics and chemistry of clouds* (Cambridge University Press, 2011).
[53]T.-W. Lee and J.-H. Ryu, "Analyses of spray break-up mechanisms using the integral form of the conservation equations," Combustion Theory and Modelling **18**, 89–100 (2014).
[54]M. El Sawi, "Distorted gas bubbles at large reynolds number," Journal of Fluid Mechanics **62**, 163–183 (1974).
[55]H. C. Simmons, "The Correlation of Drop-Size Distributions in Fuel Nozzle Sprays—Part I: The Drop-Size/Volume-Fraction Distribution," Journal of Engineering for Power **99**, 309–314 (1977).
[56]H. Zhao, H. F. Liu, J. L. Xu, and W. F. Li, "Experimental Study of Drop Size Distribution in the Bag Breakup Regime," Industrial & Engineering Chemistry Research **50**, 9767–9773 (2011).
[57]W. R. Lane, W. C. Prewett, and J. Edwards, "Some experiments on the shatter of drops by transient blasts of air," Tech. Paper (1949).
[58]W. R. Lane and R. G. Dorman, "Further experiments on the shattering of drops by a supersonic air blast," Tech. Paper (1952).
[59]W. R. Lane, "Shatter of Drops in Streams of Air," Industrial & Engineering Chemistry **43**, 1312–1317 (1951).
[60]H. Lhuissier, C. Sun, A. Prosperetti, and D. Lohse, "Drop Fragmentation at Impact onto a Bath of an Immiscible Liquid," Physical Review Letters **110**, 264503 (2013).
[61]S. Castrillon-Escobar, "Instability and dispersion of liquid jets corium: analysis of physical processes and modelling in the MC3D software," Thèse, Université de Lorraine (2016).